12-2020

Antenna Radiation Element Designs for 5G Applications

Zhijun Gui
University of Arkansas, Fayetteville

ANTENNA RADIATION ELEMENT DESIGNS FOR 5G APPLICATIONS

ANTENNA RADIATION ELEMENT DESIGNS FOR 5G APPLICATIONS

An undergraduate honors thesis
submitted in partial fulfillment of the requirements for the
Honors Studies in Electrical Engineering

By

Zhijun Gui

December 2020
University of Arkansas

Dr. Magda O. El-Shenawee
Thesis Director:

Abstract

This thesis introduced the advantage of the fifth-generation network and gave examples to the three major classes of applications categorized by International Telecommunication Union-Radiocommunication Sector. In this work, a patch antenna and a board-band bow-tie antenna with microelectromechanical switch design were modified to meet 5G communication purposes. The revised patch antenna produced a minimum S11 of -57.92dB, a resonant frequency at the 28GHz, and bandwidth of 4.55GHz. The modified design meets the requirements for wireless communication purposes. During the duplication process of the board-band bow-tie antenna design, multiple discrepancies were found, and the proposed results were not able to achieve. The possible reason for the discrepancies are analyzed, and some further works to duplicate the original design were identified.

ACKNOWLEDGEMENTS

I would first like to thank my thesis advisor Dr. El-Shenawee at the University of Arkansas. Dr. El-Shenawee was always willing to help whenever I ran into a trouble spot or had a question about my research or writing. She consistently allowed this paper to be my own work, but steered me in the right the direction whenever she thought I needed it.

I would also like to thank the people at the Terahertz Imaging and Spectroscopy Lab especially Nagma Vohra and Jose Santos. It is their enthusiasm that contagious me and motivated me.

TABLE OF CONTENTS

LIST OF FIGURES

1 Introduction

With the increasing demand for data transmission, the current 4G-LTE network cannot meet the demands of massive devices communications, high data rate and bandwidth, and low-latency. Therefore, new communication technology needs to be developed. 5G, or 5Gth, namely the fifth-generation mobile network, is one of the most popular and advanced technologies in the wireless communication field. By operating at the much higher frequency, typically more than ten times higher compared with the 4G technology, it can carry a considerably larger amount of information, provide wider bandwidth, and avoid the already crowded low-frequency band since most of the conventional wireless communication happened between 300MHz to 3GHz[1]. Figure1.1 shows the availability of Mm-wave Spectrum between 3Ghz to 300GHz, in which most of the frequency are unoccupied.

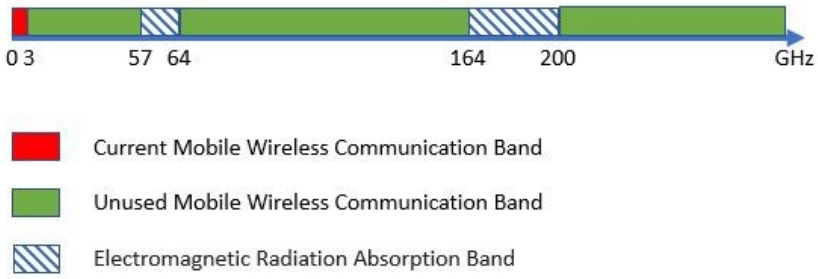

Figure 1.1: Mm-wave Spectrum Availability from 3 to 300 GHz

Thus, a communication network exploring this unused frequency band has become the most promising next-generation wireless communication technology and aims to support a wide range of applications.

1.1 5G Applications

The 5G applications were categorized by the International Telecommunication Union-Radiocommunication Sector (ITU-R) into three major classes: ultra-reliable low-latency communications (uRLLC), massive machine-type communications (mMTC), and enhanced mobile broadband (eMBB)[2]. Figure1.2 summarized the applications that lie in these three classes.

The uRLLC case requires two basic functionalities: low latency and high reliability.

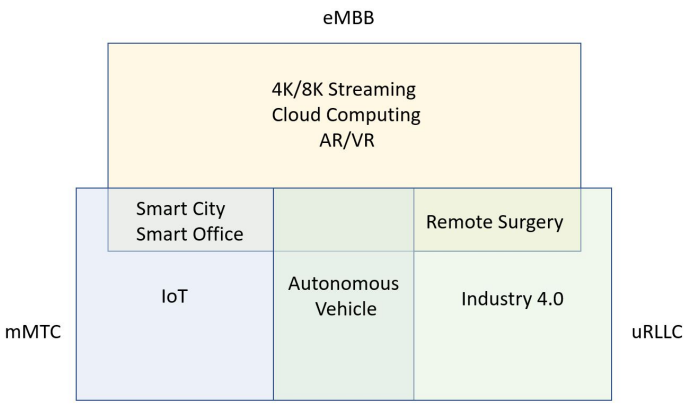

Figure 1.2: Three Major Cases of 5G Applications

Thanks to the flexible numerology and frame structure of 5G technology, the transmission time interval (TTI) of a two symbol mini-slot can be as low as 35.7μs, assuming the 60 kHz subcarrier spacing[2]. The 5G network is able to provide multi-slot repetition, which significantly enhanced the reliability of devices that can not wait for hybrid automatic repeat request (HARQ) feedback[2]. One of the application scenarios of uRLLC is autonomous vehicle networks, where low latency and high reliability are crucial for controlling a fast-moving vehicle. The latency of the current 4G-LTE technology does not satisfy the need for vehicle-to-everything (V2X) or even basic vehicle-to-vehicle (V2V) communication requirements. However, a recent study has shown that the reliability and latency are enhanced by adopting the network slicing algorithm-a potential solution for uRLLC-in autonomous vehicle networks[3].

The mMTC case is the application where a large number of devices need to be connected at once and communicate with each other. Nowadays, there are more than five billion mobile phone users, and this number this number could reach 80 billion by 2030[4]. In 2015, 3GPP Release 13 proposed an LPWAN radio technology called Narrowband Internet of Things (NB-IoT)[5]. NB-IoT technology is designed to connect billions of devices within the same network. Most of the advanced 5G wireless applications (e.g., autonomous vehicles, smart city infrastructure, and industry 4.0) will lie in the mMTC area[4]. Figure1.3 is the basic architecture of 5G IoT.

The eMBB case is the application where high data rates in a densely populated area are required. The 5G network is expected to be 100 times faster than the conventional 4G-LTE network[6], therefore enhancing user experience. With up to 20Gbps of data rates, a

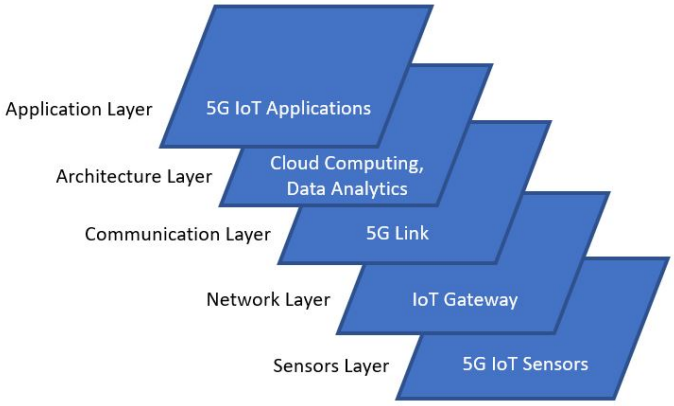

Figure 1.3: 5G IoT Architecture

5G network can support services that require colossal bandwidth, such as 4K/8K streaming, cloud computing, and Augmented reality and Virtual Reality (AR/VR)[6]. Besides the high data rate, the 5G network can also support about a hundred times higher traffic capacity than the current level[2].

1.2 Types of Antennas for 5G Applications

The development of the 5G communication system relies on a well-designed smart antenna. One of the essential characteristics of the smart antenna is the beam-forming capability. The higher frequency of the mm-wave increased the sensitivity to obstacles and interference[7], poor efficiency, and higher path loss. Using this method can focus the direction of the main beam into the optimal data-delivery route to a particular user instead of radiating into all directions, thus reducing energy consummation, dwindling the interference between users, decreasing the electromagnetic field around stations, and increasing efficiency. In addition, a smart antenna should serve the purpose of the space-division multiple access (i.e., SDMA) method, which also requires a relatively narrow main beam[8]. Therefore, a 5G antenna design should achieve the best directional gains[9]. One perfect example of antennas with a high directional gain is the horn antenna. A large-scale horn antenna system can deliver a combination of high directional gain and steerable and narrow main beam[10]. In December 2011, Sridhar Rajagopal proposed a horn antenna array which delivered a gain of 26.28 dBi and is able to steer $\pm 45^{\circ}$ in the azimuth and $\pm 10^{\circ}$ in the elevation[11]. The area of the 12×4 array is about 11.66cm $\times$ 6.81cm[11]. Figure1.4a is an example of the mmWave

transceiver system using the horn antennas. However, the antenna's size is strictly limited for the cell phone applications, so the horn antenna array is infeasible. In May 2013, Samsung announced a 28GHz communication prototype system using 64 patch antenna array instead of the bulky horn antennas[1]. The patch antenna's size is about a half wavelength of the center frequency, in this case, 28GHz. Thus, each antenna element is about 5mm. This prototype system achieved promising results-a data rate of more than 1 Gb/s, and proves that the patch antenna array is the best option for mobile applications. Figure1.4b shows a cellphone fitted with 28GHz patch antenna array.

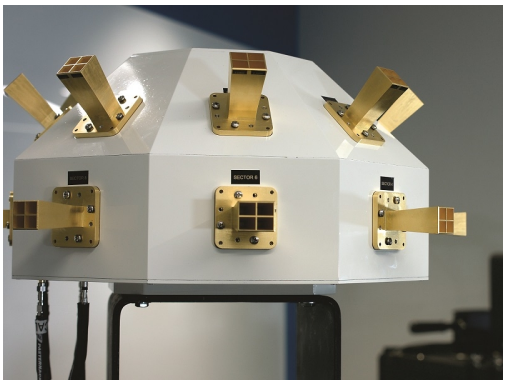

(a) AT&T Channel Sounder[12]

(b) Samsung Prototype Cellphone[1]

Figure 1.4: Two Types of Antenna for 5G Applications

In this paper, a rectangular patch antenna and a bow-tie antenna were modified in order to meet the 5G requirement. The patch antenna was modified such that the center frequency is at 28GHz, which is one of the main frequency bands assigned for 5G applications by Federal Communications Commission. Both antennas were simulated using High-Frequency Structure Simulator® (i.e. HFSS).

1.3 Summary

The novel fifth-generation network can provide three major classes of applications, including uRLLC, mMTC, and eMBB. With these advanced characteristics, the 5G network is expected to provide high data rates, low latency, and connect a massive number of devices. The essential requirement of the smart antenna is massive Multi-input Multi-output (mMIMO) and beam-forming capability. The patch antenna had proved to be the optimal option for the 5G network.

2 Patch Antenna

The patch antenna is a type of resonant antennas often used in wireless communication. The nature of the feeding network limited the bandwidth of the patch antenna and subsequently limited the applications of the patch antenna. However, the patch antenna still offers numerous advantages such as small physical profile, easy to fabricate, and low cost. The patch antenna is built on a PCB substrate with copper cladding on both sides, where the top side will be milled into the shape of the antenna (i.e., the patch) and the bottom side will serve as a ground plane. The patch antenna is usually excited either feeding from the bottom of the antenna through a coaxial probe or from the edge through a coplanar waveguide or microstrip. Thus, despite some disadvantages, the patch antenna is still one of the best antennas for cell phone applications, especially when an array of antennas is needed to satisfy the 5G beam-forming and massive MIMO characteristic since most other types of antennas will have trouble fitting into the limited space. Figure2.1 shows multiple patch antennas that were fabricated on a printed circuit board.

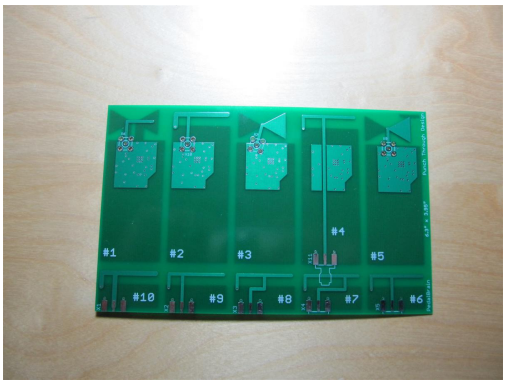

Figure 2.1: Patch Antennas on PCB[13]

2.1 Patch Antenna Theory

Patch antennas can be any shape, while the most basic one is the rectangular shape. Figure2.10 demonstrates the dimension of a typical rectangular shape patch antenna, where W is the width of the patch, L is the length of the patch, t is the high of the dielectric substrate and ε_r is the relative permittivity of the dielectric substrate.

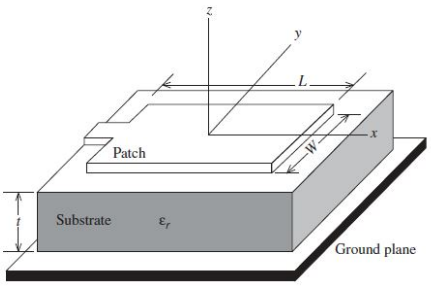

Figure 2.2: Dimensions of Patch Antenna[14]

To achieve the high efficiency, the input impedance of the antenna should be matched to the characteristic impedance of the input transmission line, which is usually 50+j0 Ω. The mismatched input impedance can distort the incoming energy and ultimately lead to a low radiation efficiency. In order to optimize the efficiency, Equation(2.1) can be used to calculate the width of the patch.

$$W = \frac{\lambda}{2}\left[\frac{\varepsilon_r + 1}{2}\right]^{-1/2} \tag{2.1}$$

One method to find the length of the patch is to use the half-wave patch model, where L can be approximate by the half wavelength of the dielectric substrate[14]. By using this method, one can use Equation(2.2) to calculate the length. The reason why a coefficient of 0.49 is used instead of 0.5 is because of the fringing effect of the patch. The fringing electrical field at the edge of the patch makes the patch appear larger electrically than physically as shown in Figure2.3. Thus, a 0.49 was used to compensate for this effect.

$$L \approx 0.49\lambda_d = 0.49\frac{\lambda}{\sqrt{\varepsilon_r}} \tag{2.2}$$

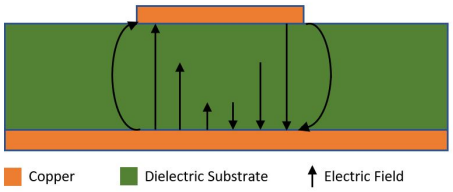

Figure 2.3: Patch Fringing Effect[15]

Although the half-wave patch model is mathematically easy to solve, this model was based on an assumed amount of fringing effect and did not include some critical parameters

such as the width of the patch and the height of the substrate, which plays an essential role in affecting the resonant frequency. Warren L. Stutzman argues that the cavity model is more adaptable than the transmission-line model, which is another primary analytical method. He suggested that the cavity mode can be applied to antennas not limited to the rectangular patch but many other shapes while providing higher accuracy compared with the conventional half-wave patch model[14]. The cavity model starts with a modified half-wave patch model, as shown in Equation(2.3), which calculated the fringing effect using W and t. [16].

$$L = 0.5\frac{\lambda}{\sqrt{\varepsilon_r}} - 2\Delta L \tag{2.3}$$

where ΔL is the fringing length can be found from W and t as

$$\Delta L = 0.412\frac{(\varepsilon_{re} + 0.3)\left(\frac{W}{t} + 0.264\right)}{(\varepsilon_{re} - 0.258)\left(\frac{W}{t} + 0.8\right)}t \tag{2.4}$$

where ε_{re} is the effective dielectric constant can be found from W, t and relative permittivity of the substrate ε_r as

$$\varepsilon_{re} = \frac{\varepsilon_r + 1}{2} + \frac{\varepsilon_r - 1}{2}\left(1 + \frac{10t}{W}\right)^{-0.5} \tag{2.5}$$

2.2 Phased-Array Analysis

There are eight major requirements summarized by Mamta Agiwal[17], the two that most related to the antenna radiating element are high bandwidth and a significant reduction in energy consummation (almost 90%). To reduce the energy consumption while still providing optimal signal strength, the 5G antenna array should produce the narrow beam so energy can be transmitted into one direction. The array will also have the ability to steer the high directional beam by using the phase shifters in order to focus the beam onto a particular direction[18]. The overall radiation pattern of any phased-array is the product of the radiation pattern of a single element and the array factor. According to Warren L. Stutzman, author of the book *Antenna Theory and Design*, a planar wave hitting a receiver array with N element at an angle of θ produced a phase delay of ξ_n onto each element. The array factor (i.e., AF) is found as the sum of the product of the antenna response and the complex currents of each element shown in Equation(2.6)[14].

$$AF = I_0 e^{j\xi_0} + I_1 e^{j\xi_1} + ... + I_{N-1} e^{j\xi_{N-1}} = \sum_{n=0}^{N-1} I_n e^{j\xi_n} \tag{2.6}$$

Now, change the complex current to the product of its magnitude and phase, that is, $I_n = A_n e^{jn\alpha}$, as well as express the phase difference ξ in terms of the physical distant d difference between each element, that is, $\xi = \beta d \cos\theta$[14]. Since the phase difference between any two adjacent elements is $\beta d \cos\theta$, assuming $\xi_0 = 0$, we have

$$AF = \sum_{n=0}^{N-1} A_n e^{jn\alpha} e^{j\beta nd\cos\theta} = \sum_{n=0}^{N-1} A_n e^{jn(\beta d\cos\theta+\alpha)} \tag{2.7}$$

Assuming a uniformly excited, equally spaced linear array, where the distance between each element is d and the complex current is I_0, and define $\psi = \beta d\cos\theta + \alpha$, we have

$$AF = \sum_{n=0}^{N-1} A_0 e^{jn(\beta d\cos\theta+\alpha)} = \sum_{n=0}^{N-1} A_0 e^{jn\psi} \tag{2.8}$$

However, the linear array can only steer the beam into the direction along the line. Thus, in practice, a two-dimensional array is usually used, more specifically, a circular, rectangular, or square planar array[14]. The geometry of a typical rectangular planar array is shown as Figure2.4. The array factor of this type of array is given by multiplication of two array factors, one in the x-direction(M elements) and one in the y-direction(N elements) as indicated in Figure2.4. The combined array factor is[14]

$$AF(\theta,\phi) = \sum_{m=1}^{M} I_{xm} e^{j\xi_{xm}} \times \sum_{n=1}^{N} I_{yn} e^{j\xi_{yn}} \tag{2.9}$$

where

$$\xi_{xm} = \beta x'_m \sin\theta\cos\phi \qquad \text{and} \qquad \xi_{yn} = \beta y'_n \sin\theta\cos\phi \tag{2.10}$$

For a uniformly excited array(i.e., identical current magnitude I_0 and identical phase shift α), this equation can be simplify down to

$$AF(\theta,\phi) = I_0 \left[\sum_{m=1}^{M} e^{j(\beta x'_m \sin\theta\cos\phi+m\alpha)} \times \sum_{n=1}^{N} e^{j(\beta y'_n \sin\theta\cos\phi+n\alpha)}\right] \tag{2.11}$$

Figure2.5a and Figure2.5b is the radiation pattern of a phased-array with 60 ° and 90° scanning angle,respectively.

2.3 Design Procedure

There are a few constraint need to be met when designing a patch antenna for communication purpose. The voltage standing wave ratio (VSWR) needs to be small than 3 at

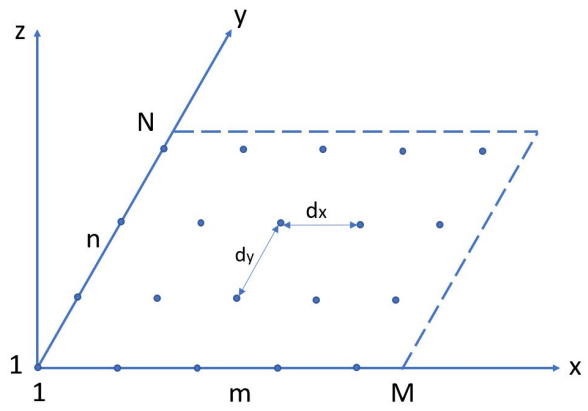

Figure 2.4: Geometry of Rectangular Planar Array

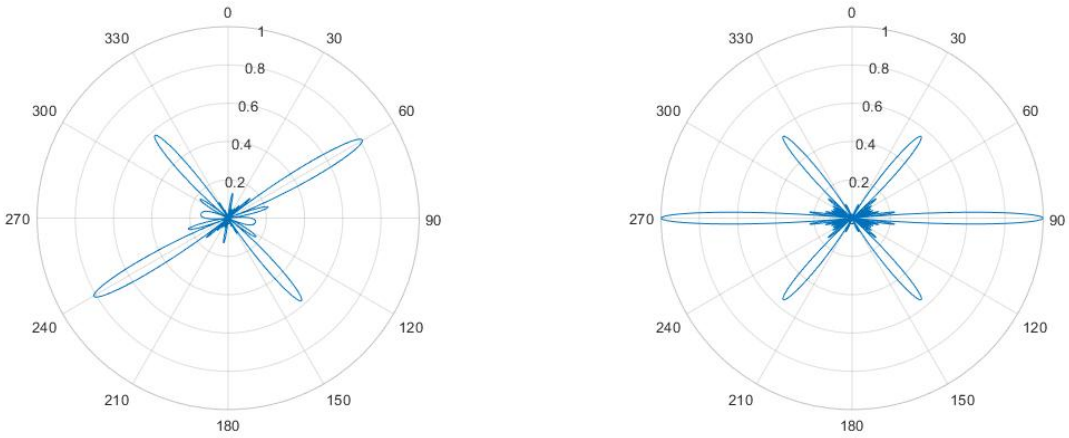

(a) 60° Scanning Angle

(b) 90° Scanning Angle

Figure 2.5: Phased-Array Scanning

the operating frequency 28GHz, antenna gain greater than 0dBi, radiation efficiency greater than 50%, and bandwidth greater than 8%[14]. A design was used as a reference from the webcast *Design and Simulation of 5G 28-GHz Phased-Array Transceiver Webcast* by Jack Sifri[19]. Figure2.6a is the original dimension and performance of the antenna, which provides a resonant frequency at 27.5GHz with -28dB return loss and bandwidth of 2Ghz with respect to the -10dB threshold. This antenna is then modified to achieve a better performance, including broader bandwidth, lower return loss, and resonant exactly at 28GHz. Four variables were assigned to the patch; they are feed_x, feed_y, insert_x, and insert_y. Please refer to Figure2.6b for the edge where those variables were assigned to. During the

modification, each of the variables was adjusted while the length and width of the patch and the material of the substrate were left unchanged. The high of the substrate was also modified, and the influence on the S11 was recorded.

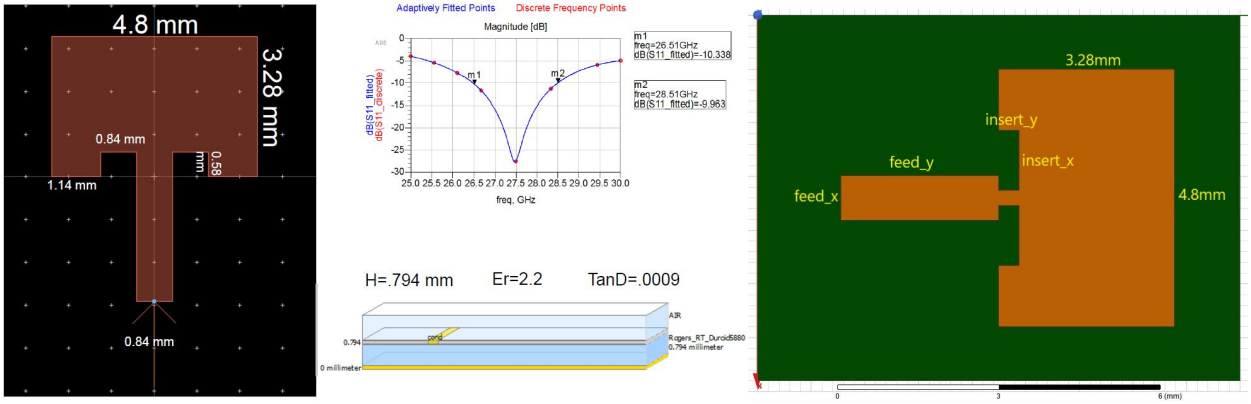

(a) Reference Patch Design (b) Patch Variables

Figure 2.6: Antenna Patch Reference Design and Variables

To analyze which variable effects S11 the most under which frequency, one can use an analytic derivatives plot as a reference. Figure2.7 is the analytic derivatives plot of the four variables plus the high of the substrate. The plot provided the partial derivative of the magnitude of the S11 with respect to that variable across the interested frequency range.

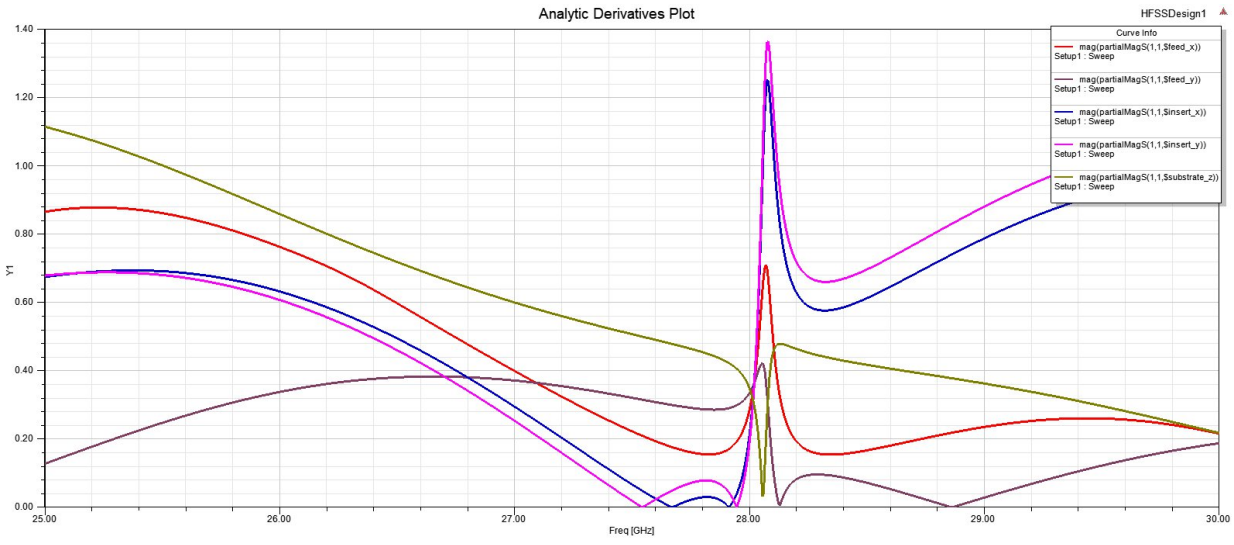

Figure 2.7: Analytic Derivatives Showing the Sensitivity of Variables

According to this plot, the high of the substrate plays a most important role but gradually

decreases the weight through the entire frequency of interest until outstripped by other variables. However, the effect plummeted to near zero at the resonant frequency indicates that the high of the substrate has nothing to do with how low the return loss is. Other than the high of the substrate, each variable's effect is rotational symmetry about the resonant frequency. Looking at the peaks at the resonant frequency, the weight of the effect of individual variable contributes to the return loss ranking from high to low: insert_y, insert_x, feed_x, feed_y, and substrate high. The variables insert_y and insert_x can make relative larger changes to the return loss compare with other variables. Thus, these two variables should be first to be considered when adjusting the magnitude of return loss. Figure2.8 shows the S11 by sweeping the insert_y from 0.2mm to 0.4mm, 0.02mm each step. The S11 produced a local minimum at about 28.03GHz. As the increase of the variable, the lower frequency part of the S11 curve changed about 4dB in magnitude, while the higher frequency changed more than 7dB in magnitude. Around the resonant frequency, the S11 changed the most, from -13dB to -39dB. Thus, the S11 parametric result is consistent with the analytic derivatives plot. A finer parametric was performed and found insert_y=0.37mm to be the optimal point. The variable insert_x has the same behavior since their analytic derivatives plots are similar. A parametric was performed and found the optimal length of insert_x is 1.12mm.

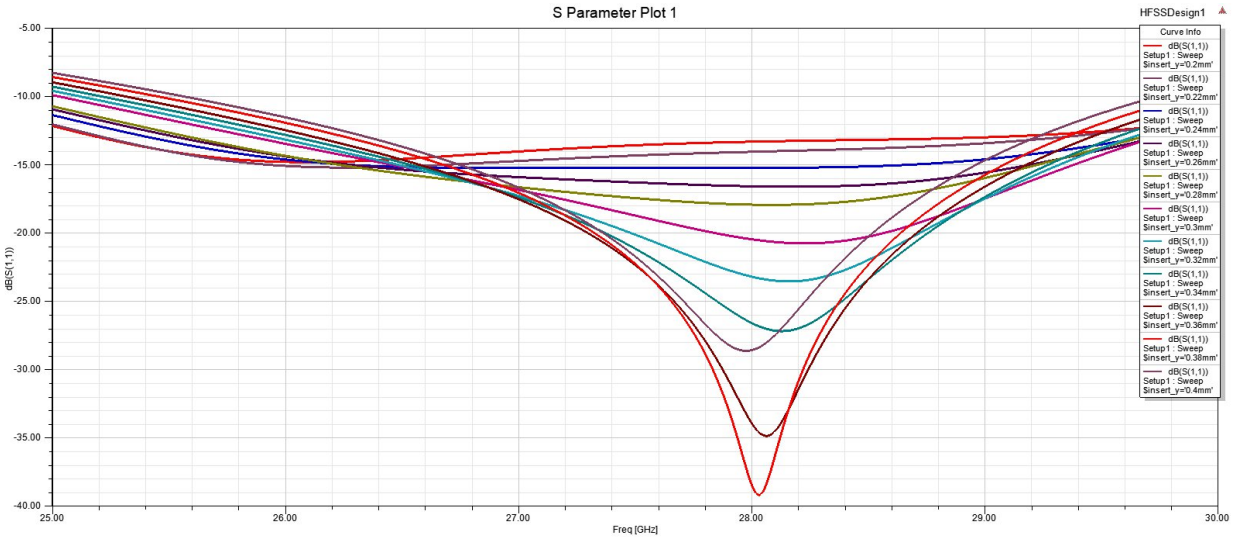

Figure 2.8: Variable Sweep Showing Best S11 Achieved at Insert_y=0.37mm

Although the modification in both insert variables produces a similar change, the

effect of changing two feed variables are very different. Thus, these two variables should be analyzed separately. Since feed_x and feed_y combined might not achieve the overall optimal at each individual's optimal point, these two variables should be analyzed together. A 2D matrix was created by sweeping feed_x from 0.35mm to 0.55mm. 0.01mm each step and feed_y from 2.95mm to 3.15mm, 0.01mm each step. The result was plotted in the three-dimensional space shown as Figure2.9, where the x- and y-axis are the sweeping variables feed_x and feed_y, and the z-axis is the return loss at 28GHz. According to this result, the S11 achieved optimal when feed_x and feed_y equal 0.42mm and 2.96mm, respectively.

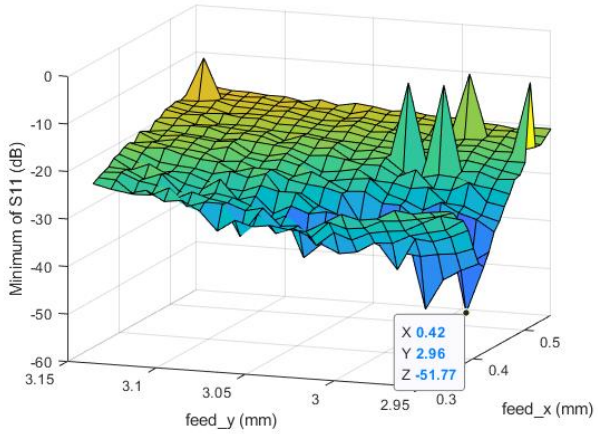

Figure 2.9: Variables Sweep Showing Best S11 Achieved at feed_x,y=0.42 and 2.96mm

Figure2.10 shows the dimension of the patch.

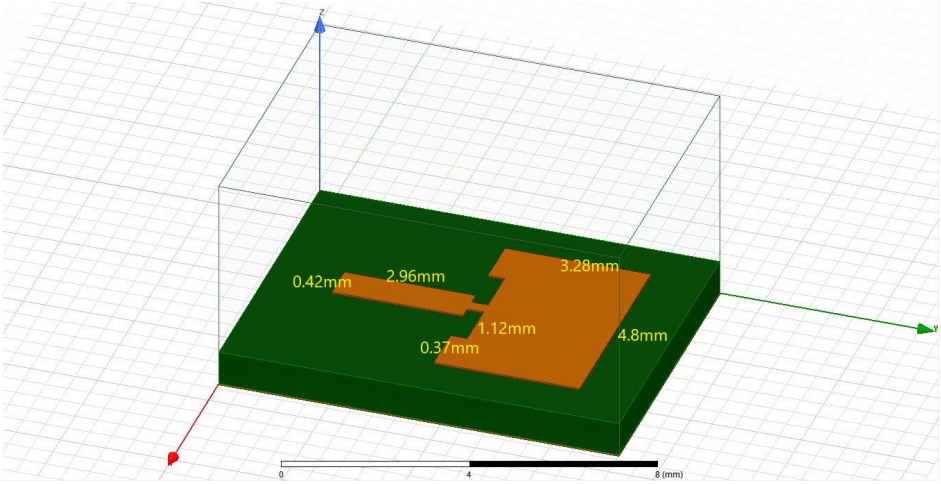

Figure 2.10: Dimension of the Patch

2.4 Antenna Simulation Result

This antenna's final design yields a minimum S11 of -57.92dB and a resonant frequency at the 28GHz. The bandwidth corresponding to the -10dB thresholds is 4.55GHz, as shown in Figure2.11. The very low return loss at the resonant frequency helps reduce the consumption of energy provided by the feeding network at a fixed output level and therefore, increases the antenna's radiation efficiency. Also, the resonant frequency of this antenna design is perfectly matched with its operating frequency, so the antenna is working at its optimal frequency. According to the antenna parameter computed by HFSS®, at the resonant frequency, this antenna produced 98.57% of radiation efficiency.

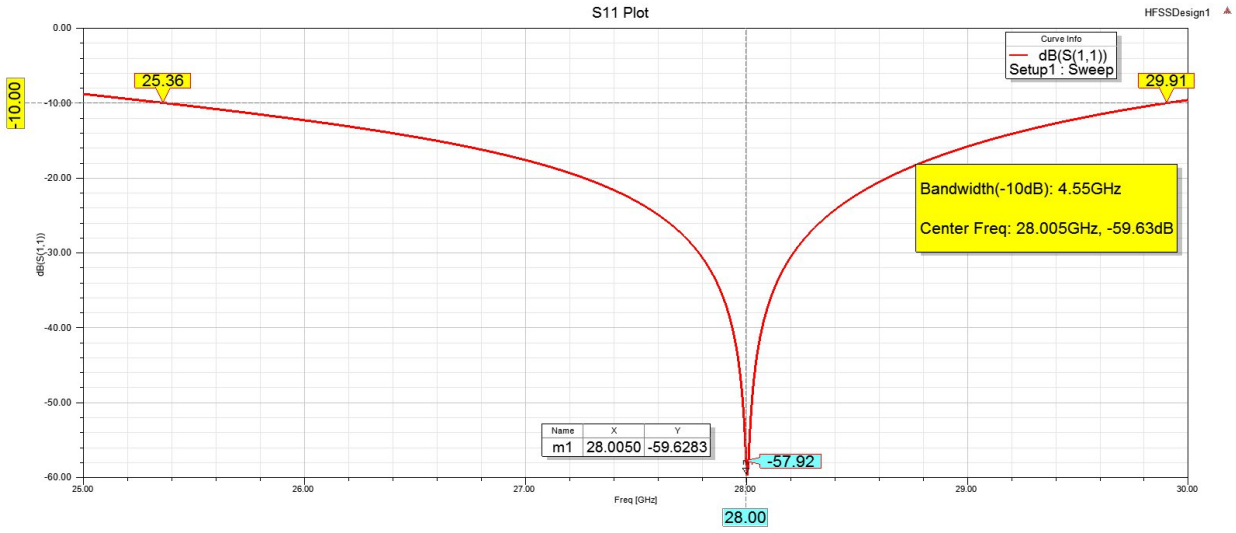

Figure 2.11: The S11 Versus Frequency Plot Showing a Resonant Frequency at 28GHz with the S11 of -57.92dB

Figure2.12a shows the voltage standing wave ratio (i.e., VSWR) and Figure2.12b shows the input impedance of this antenna design. This antenna has a VSWR lower than 3 over the entire range of frequency of interest (from 25GHz to 30GHz) and a VSWR lower than 1.5 from 26.4GHz to 29.22GHz. Thus, the impedance matching of this antenna meets the requirement for communication purposes suggested by Warren L. Stutzman[14], where VSWR should be lower than 3. This antenna can still provide a bandwidth of 2.82GHz if the VSWR threshold of 1.5 is preferred. The input impedance of the antenna is relatively smooth over the frequency range, contributing to the better matching condition and consequently, wider bandwidth. The impedance matching is designed for a transmission line with

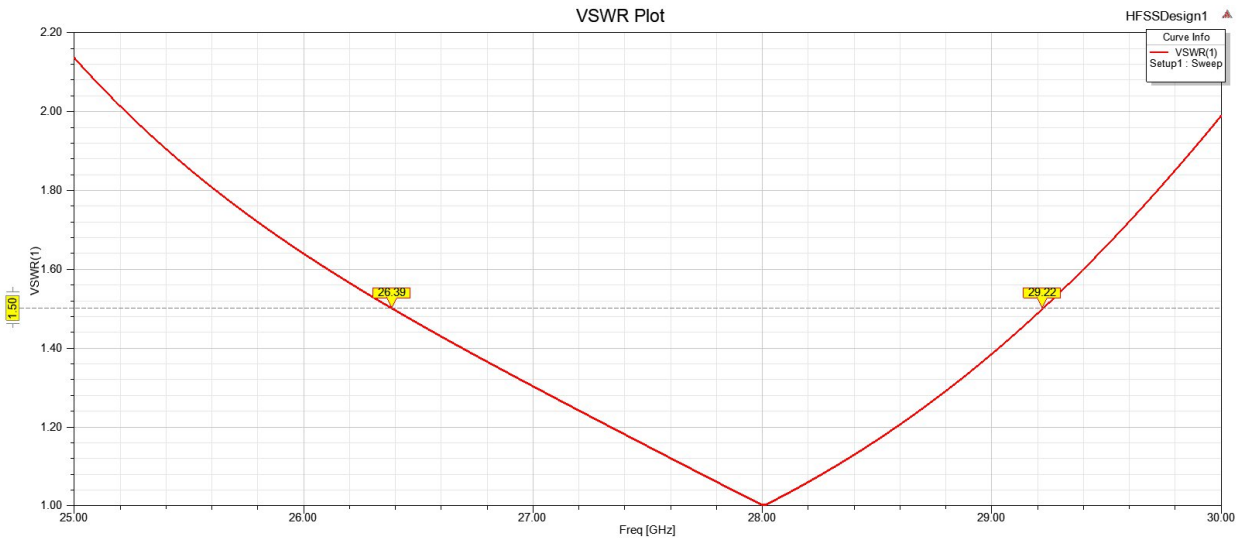

(a) VSWR Versus Frequency Plot Showing the 2.82GHz Bandwidth

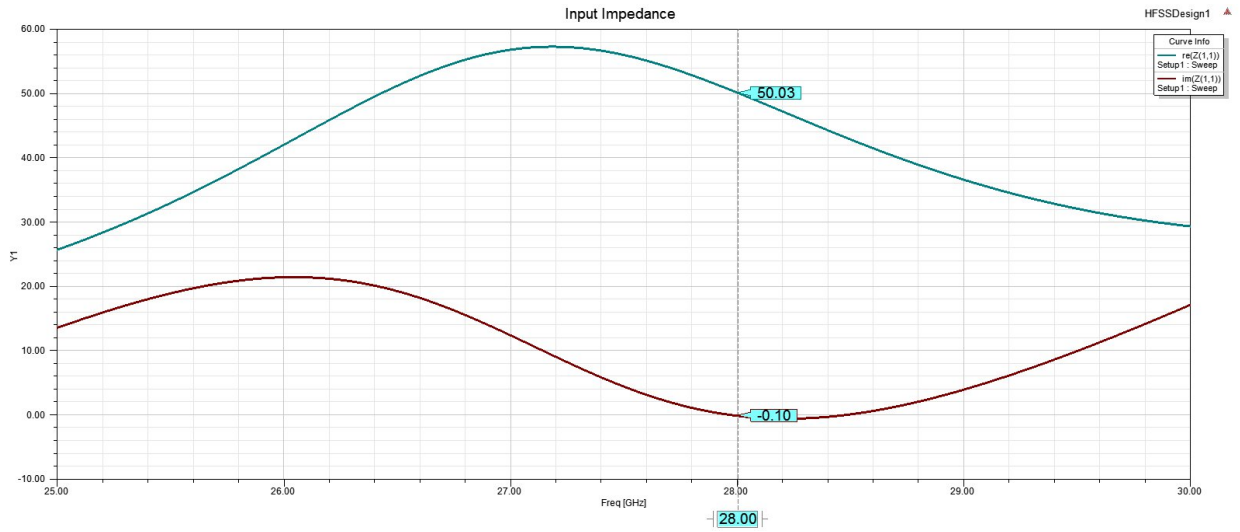

(b) Input Impedance Plot Showing $Z_{in} = 50.03 - j0.1\Omega$ at the Center Frequency

Figure 2.12: Antenna VSWR and Input Impedance

a characteristic impedance of 50+j0Ω.

Figure2.13a and Figure2.13b is the gain in dBi and the magnitude of the directivity of this antenna, in 0° and 90° azimuth angle. The maximum gain occurs at 0° polar angle with a value of 4.3dBi at the 0° azimuth and occurs at 337° polar angle with a value of 5.29dBi. The maximum directivity occurs at 0° polar angle with a value of 2.73 at the 0° azimuth and occurs at 337° polar angle with a value of 3.4. The relative high directivity provides the ability to focus the beam onto one particular user and thus reduce energy consumption.

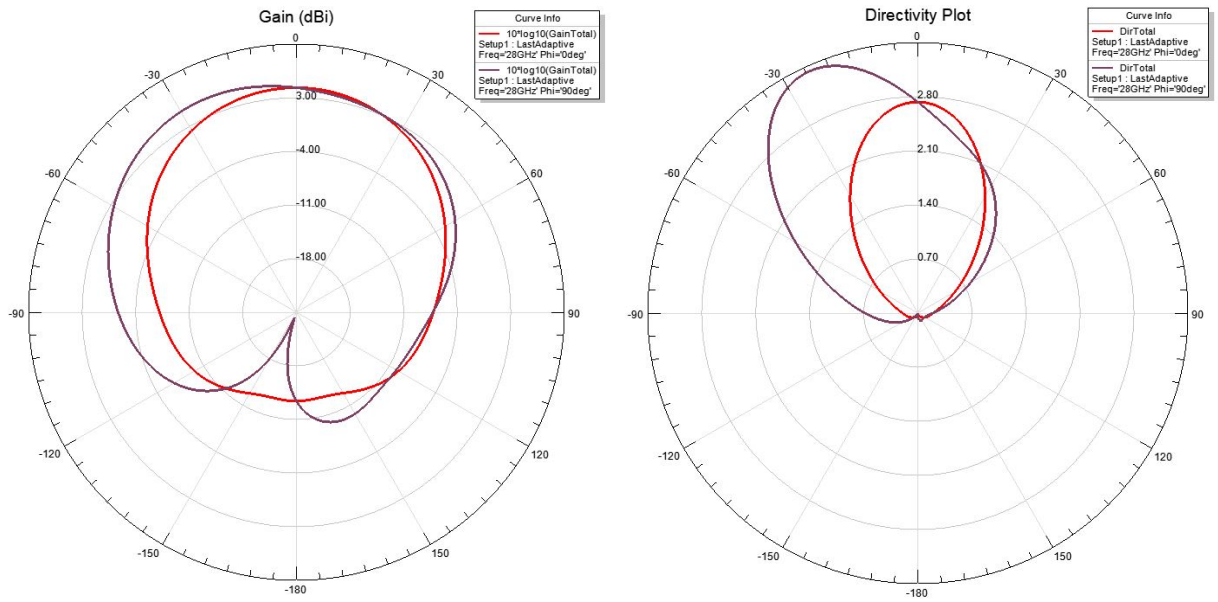

(a) Gain Plot Showing a Maximum Gain of 5.29dBi

(b) Directivity Plot Showing a Maximum Directivity of 3.4

Figure 2.13: Antenna Gain and Reactivity

Figure2.14 shows the 3D power radiation pattern of this antenna.

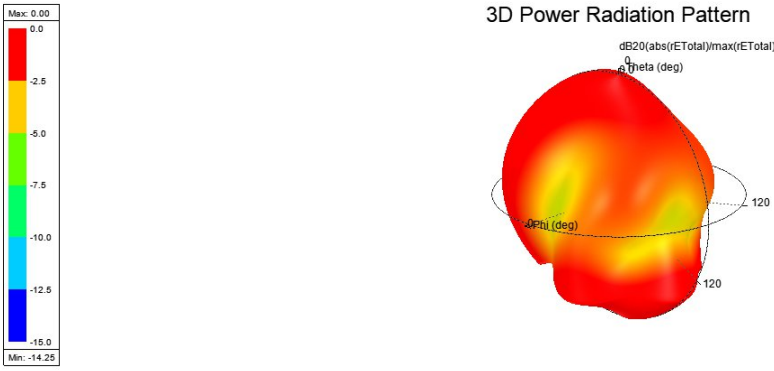

Figure 2.14: 3D Power Radiation Pattern

2.5 Summary

This chapter introduced the principle of the printed patch antenna: one of the most popular 5G antenna types. The theory of the patch antenna and antenna array was shown.

Next, a patch antenna radiating element with an insert feed was modified to meet the 5G requirements. The modified design demonstrated a minimum S11 of -57.92dB, a resonant frequency at the 28GHz, and bandwidth of 4.55GHz. The revised design produced a better performance than the original design and satisfied wireless communication purposes.

3 Bow-Tie Antenna

The bow-tie antenna, or bifin antenna, is also a type of printed low profile antenna usually fabricated on a printed circuit board. The bow-tie antenna is the planar version of the finite bi-conical antenna with a linear polarization[14]. In this project, a MEMS antenna designed by Douglas Hutchings[20] was used as a reference. The goal is to duplicate the design and modify it to meet the 28GHz center frequency while persisting the wide bandwidth. Figure3.1 shows the dimensions of the original design. In this project, only the horizontal element was simulated.

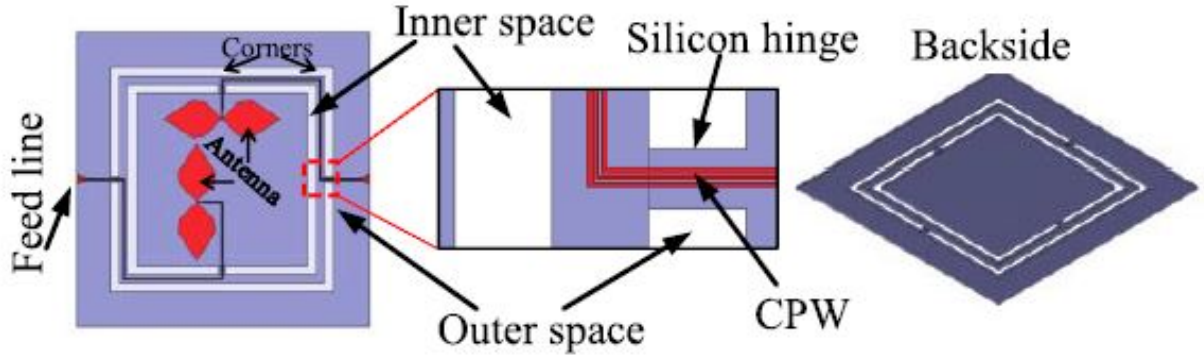

Figure 3.1: Dimensions of Original Design[20]

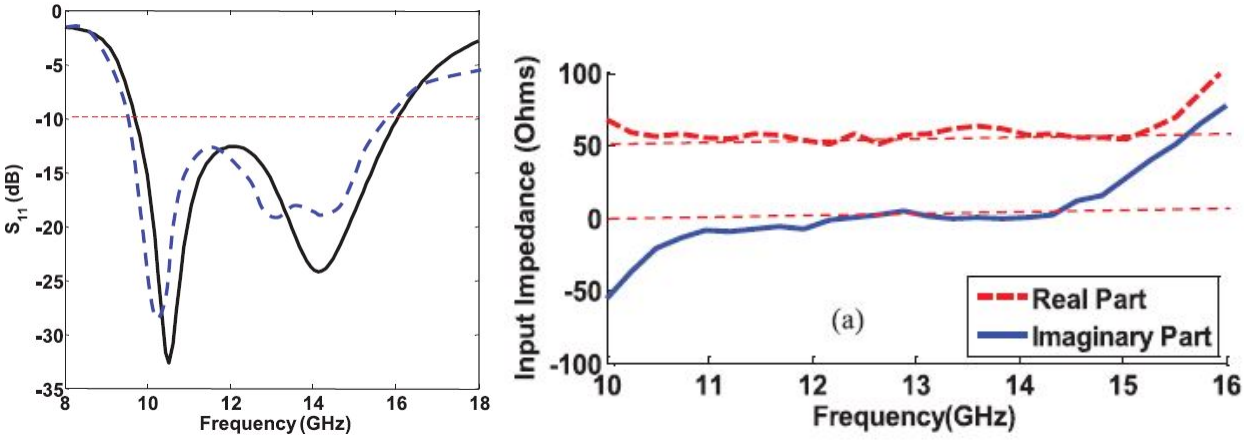

(a) S11 of Original Design (b) Input Impedance of Original Design

Figure 3.2: S11 and Input Impedance of Original Design[20]

3.1 Coplanar Waveguide Theory

In the original design, the coplanar waveguide was used to transmit the signal from the edge feed coaxial port to the radiating element. Coplanar waveguide (i.e., CPW), is a type of transmission line that consisted of a center signal strip paralleled by two ground strips on left and right with a gap. The conductor strips are built on a dielectric substrate while a ground plane may or may not required[21]. The characteristic impedance of the CPW is determined by the ratio of the signal strip's width to the width of the signal strip plus the width of two gaps between ground strip, also known as a/b ratio, given the thickness and permittivity of the substrate remain constant. In this project, a double layer dielectric substrate was used. The top layer is a $3\mu m$ silicon dioxide with relative permittivity of 4.5, and the bottom layer is a $50\mu m$ silicon with relative permittivity of 11.9. Figure3.3 shows the geometry of this configuration of CPW.

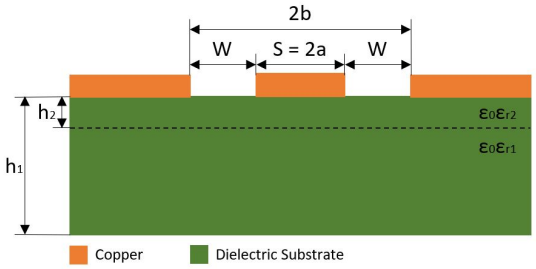

Figure 3.3: Geometry of the CPW[21]

According to Rainee Simons, author of the book *Coplanar waveguide circuits, components, and systems*, the characteristic impedance of this configuration of CPW can be calculated as Equation(3.1).

$$Z_0 = \frac{30\pi}{\sqrt{\varepsilon_{eff}}} \frac{K(k_0')}{K(k_0)} \tag{3.1}$$

where K is the complete elliptic integrals and

$$K(x) = \int_0^{\frac{\pi}{2}} \frac{1}{\sqrt{1 - x * \sin^2(\theta)}} d\theta \tag{3.2}$$

$$k_0 = \frac{S}{S + 2W} \qquad k_0' = \sqrt{1 - k_0^2} \tag{3.3}$$

The effective permittivity ε_{eff} is given by

$$\varepsilon_{eff} = 1 + q_1(\varepsilon_{r1} - 1) + q_2(\varepsilon_{r2} - \varepsilon_{r1}) \tag{3.4}$$

where q_1 and q_2 are defined as

$$q_1 = \frac{1}{2}\frac{K(k_1)K(k_0')}{K(k_1')K(k_0)} \qquad \text{and} \qquad q_1 = \frac{1}{2}\frac{K(k_2)K(k_0')}{K(k_2')K(k_0)} \tag{3.5}$$

in which

$$k_1 = \frac{\sinh\left(\pi S/4h_1\right)}{\sinh\left\{\left[\pi(S+2W)\right]/4h_1\right\}} \qquad \text{and} \qquad k_1' = \sqrt{1-k_1^2} \tag{3.6}$$

$$k_2 = \frac{\sinh\left(\pi S/4h_2\right)}{\sinh\left\{\left[\pi(S+2W)\right]/4h_2\right\}} \qquad \text{and} \qquad k_2' = \sqrt{1-k_2^2} \tag{3.7}$$

3.2 Design Procedure

In order to duplicate the original design, Figure3.4a was used as a reference. However, the dimensions given in this figure were not sufficient to recreate the geometry. Thus, AutoCAD® was used to measure the angle ∠CDA and solve the rest of the dimensions using trigonometric identities, assuming Figure3.4a was drawn to scale. The cross-section of the duplicated design was following Figure3.4b, in which the thickness of the copper cladding labeled in red is $2\mu m$.

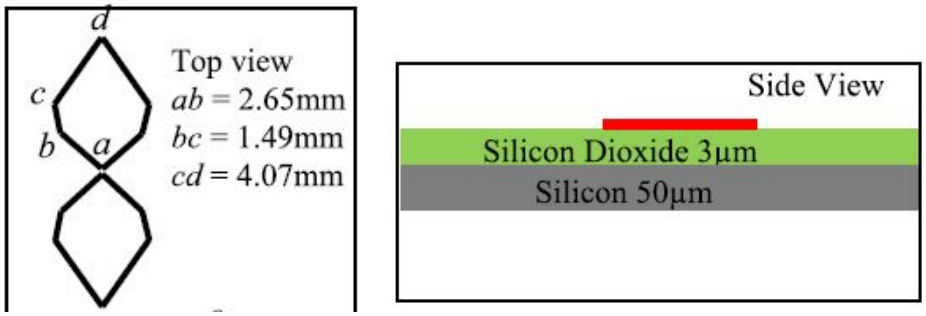

(a) Top View of Original Design (b) Side View of Original Design

Figure 3.4: Top and Side Views of Original Design[20]

Figure3.5 shows the calculated dimensions of the patch in millimeter, which contains all the dimensions necessary to recreate the patch. According to Figure3.5, the length $|ad|$ is 6.73mm long. Therefore, the wingspan across two fins of the bow-tie antenna is greater than 13.46mm. According to Douglas, the antenna was placed on a $9mm \times 9mm$ square platform[20], which is even smaller than the patch itself. Thus, the patch of the original design must not be the same with Figure3.5, perhaps shrank to some unknown scale. Assuming the edges of the inner platform is 9mm. By measuring the length $|cd|$, which is about 1.86mm according to

Figure3.1, the scaling factor can be found as the ratio of two $|cd|$ which is about 0.457. The duplicated design followed this scaling factor.

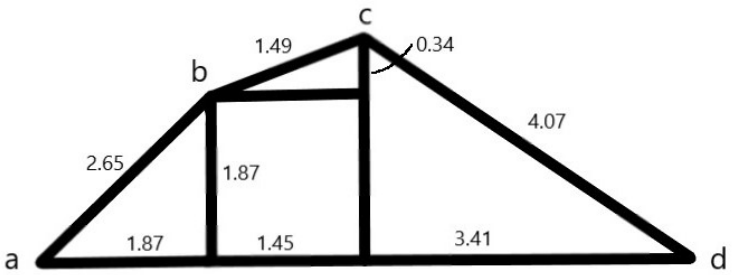

Figure 3.5: Calculated Dimension of The Patch

Besides the patch, another important element is the CPW feedline. According to Douglas, the CPW was designed with a signal line width(S) of $15\mu m$, a spacing(W) of $9\mu m$, and a ground width of $25\mu m$, where the characteristic impedance of the CPW was 50Ω[20]. However, the actual image of the actual antenna revealed a different CPW dimension compared with the proposed one. Figure3.6b is the constructed CPW according to the dimensions listed above, while Figure3.6a is the image of the CPW of the actual antenna.

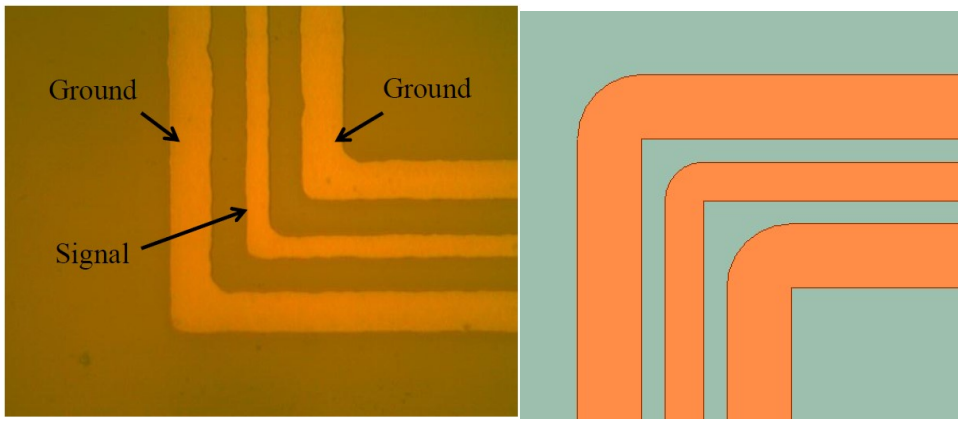

(a) Image of Actual CPW[22] (b) Proposed CPW Geometric

Figure 3.6: Actual CPW Geometric vs. Proposed CPW Geometric

The spacing between the two grounds is noticeably wider than the proposed dimensions. Although the dimensions can not be directly measured from the image, since it is the a/b ratio that controlled the characteristic impedance, it is feasible to take the ratio without warring about the actual dimensions. By measuring the S and W from the image

using AutoCAD®, the a/b ratio of actual CPW is about 0.25. In contrast, the a/b ratio of the proposed dimensions is about 0.45. It is even more perplexing considering the CPW theory introduced in Section3.1, which suggests an a/b ratio of about 0.6 in order to achieve a 50Ω characteristic impedance. Figure3.7a and Figure3.7b is the relationship of a/b ratio and spacing to the characteristic impedance calculated using the CPW theory. Both the characteristic impedance of the proposed and actual a/b ratio deviated from 50Ω.

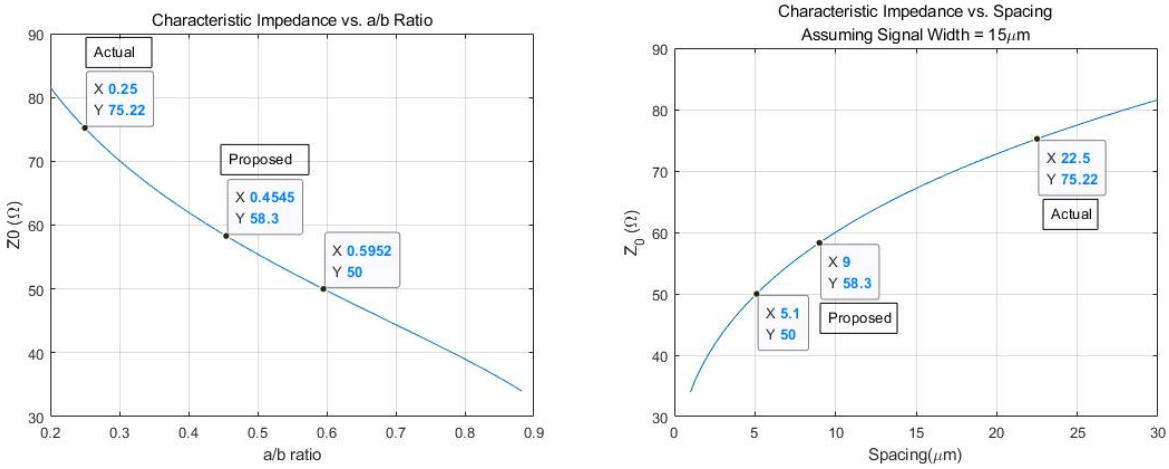

(a) Z_0 Versus a/b Ratio

(b) Z_0 Versus Spacing

Figure 3.7: Characteristic Impedance Versus a/b Ratio and Spacing Showing the Discrepancy Among Actual, Proposed, and Theory CPW Design

Since the original design was fabricated and the testing result is coherent with the simulation result, the a/b ratio of 0.25 measured from the image of actual CPW was used. The width of the signal line was assumed to be $15\mu m$, which implies the spacing to be $22.5\mu m$. The rounded corner design of the CPW was used because the actual fabrication tends to produce a rounded corner than straight.

In the original design, an SMA connector was used to excite the antenna. Due to the diameter of the center and the relatively narrow CPW signal line, a transition was designed from the CPW to the SMA connector. This design was recreated, and the SMA connector was also modeled based on the manufacture datasheet. In order to precisely excite the antenna, a wave port excitation method was chosen. Figure3.8 shows the duplicated design in HFSS®. The dimensions of the rotation hinges, the SMA-CPW transition, and the outer frame were measured from Figure3.1 using AutoCAD®, assuming the edges of the inner

platform is 9mm long.

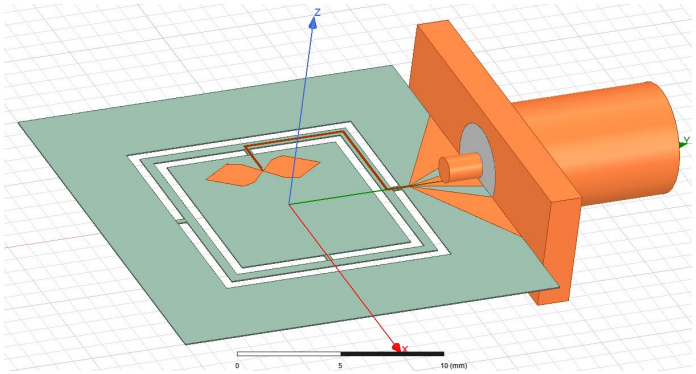

Figure 3.8: Geometric of Duplicated Design

3.3 Antenna Simulation Result

The simulation results of the duplication result show a discrepancy with the original design. Figure3.9 compares the S11 of the original design simulation, original design measurement, and duplicated design. According to this figure, the duplicated design resonated at the 17.65GHz, which is higher than the original design, which is about 10.5 GHz. It is possible that this higher resonate frequency was introduced by the scaling of the patch size.

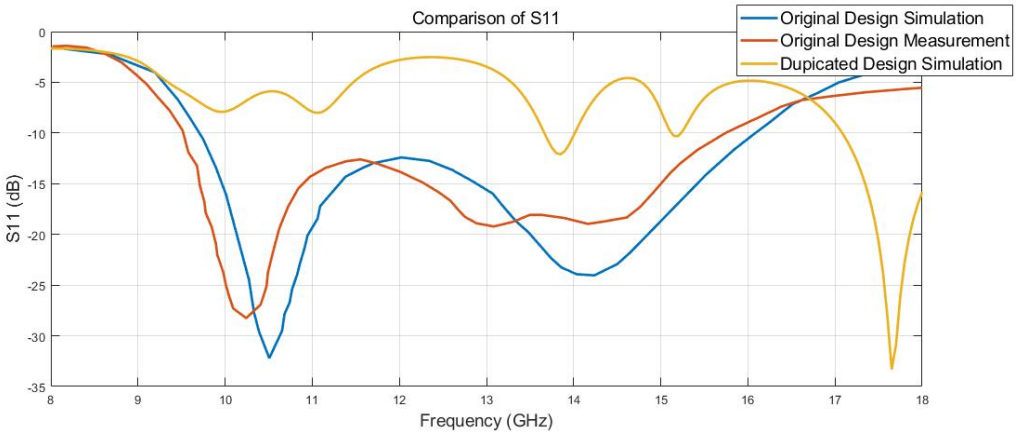

Figure 3.9: S11 Versus Frequency Plot Showing the Difference Among Original Deign Simulation and Measurement , and Duplicated Design Simulation Results

Figure3.10 shows the input impedance of the duplicated design. According to this

figure, the matching was distorted, compares to the original input impedance Figure3.2b. This mismatch could be caused by the spacing of the CPW, which has the confusion. The curve is relatively flat at the higher frequency range, suggest that the antenna might be shrunk to a smaller scale than the original design.

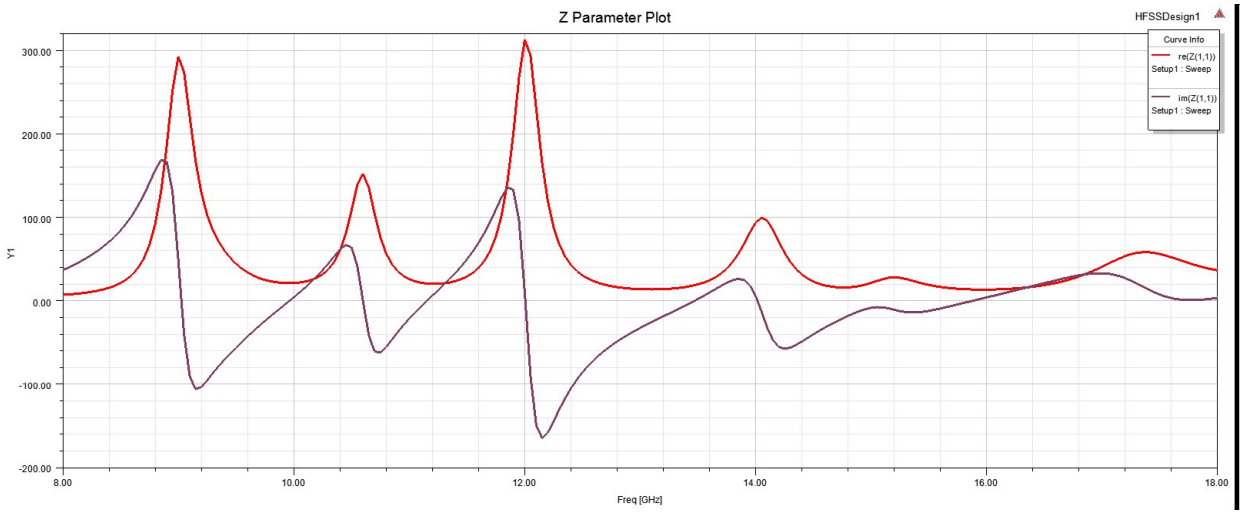

Figure 3.10: Input Impedance Versus Frequency Plot Showing the Non-Smooth Input Impedance Over Frequency of Interest

The duplicated designed made based on the claim that the edge of the inner platform is 9mm, and the patch was therefore scaled accordingly, so the patch is able to fit correctly. However, since the duplicated design shows a higher resonant frequency, which is directly proportional to the patch's size, the size of the inner platform is questionable. It is also possible that the measuring process introduced tolerance. Most of the duplication models' dimensions are measured directly from the proposed image, where measuring tolerance is unavoidable. Due to the discrepancy and presented tolerance, further analysis and simulations are needed in order to duplicate the original design.

3.4 Summary

This chapter introduced a board-band MEMS bow-tie antenna design centering at 10.8GHz made by Douglas Hutchings. The goal is to duplicate the original work and aimed to modify the design to satisfy 5G communication purposes. However, multiple discrepancies were found during the duplication process, and the originally proposed results cannot be achieved.

4 Conclusion and Further work

Chapter 1 introduced the advantage of the fifth-generation network and three major classes of applications categorized by ITU-R. An example of an application was given for each case, including uRLLC, mMTC, and eMBB. This chapter also introduced radiating elements commonly used for the 5G network and indicated that the patch antenna is the optimal one for 5G cellphone applications.

In Chapter 2, a patch antenna radiating element with an insert feed was modified. The modified design demonstrated a minimum S11 of -57.92dB, a resonant frequency at the 28GHz, and bandwidth of 4.55GHz. The revised design produced a better performance than the original one and met the requirement for wireless communication purposes. However, the array performance of this design has not been tested yet, and the 5G application requires an array of antennas. Thus, it is essential further to analyze the characteristics of this design in an array.

In Chapter 3, a design was made to duplicate the original board-band MEMS bow-tie antenna design by Douglas Hutchings and aimed to modified the duplicated design for 5G application. However, during the duplication process, multiple discrepancies were found, and the proposed results were not able to achieve. The reason could be caused by the tolerances introduced when obtaining the dimensions. Since the dimension of the antenna is highly sensitive at high frequency, the tolerances could completely distort the results. For the future, parameter sweeps need to be performed on the two significant discrepancies: the scale and the CPW a/b ratio, in order to achieve the proposed result.

Bibliography

[1] T. S. Rappaport, W. Roh, and K. Cheun, "Mobile's millimeter-wave makeover," *IEEE Spectrum*, vol. 51, no. 9, pp. 34–58, 2014.

[2] S. R. Pokhrel, J. Ding, J. Park, O. Park, and J. Choi, "Towards enabling critical mmtc: A review of urllc within mmtc," *IEEE Access*, vol. 8, pp. 131 796–131 813, 2020.

[3] X. Ge, "Ultra-reliable low-latency communications in autonomous vehicular networks," *IEEE Transactions on Vehicular Technology*, vol. 68, no. 5, pp. 5005–5016, 2019.

[4] L. Chettri and R. Bera, "A comprehensive survey on internet of things (iot) toward 5g wireless systems," *IEEE Internet of Things Journal*, vol. 7, no. 1, pp. 16–32, 2020.

[5] A. Hoglund, X. Lin, O. Liberg, A. Behravan, E. A. Yavuz, M. Van Der Zee, Y. Sui, T. Tirronen, A. Ratilainen, and D. Eriksson, "Overview of 3gpp release 14 enhanced nb-iot," *IEEE Network*, vol. 31, no. 6, pp. 16–22, 2017.

[6] W. Chen, X. Fan, and L. Chen, "A cnn-based packet classification of embb, mmtc and urllc applications for 5g," in *2019 International Conference on Intelligent Computing and its Emerging Applications (ICEA)*, 2019, pp. 140–145.

[7] T.-Y. Wu and T. Chang, "Interference reduction by millimeter wave technology for 5g-based green communications," *IEEE Access*, vol. 4, pp. 10 228–10 234, 2016.

[8] Z. Feng and Z. Zhang, "Dynamic spatial channel assignment for smart antenna," *Wireless Personal Communications*, vol. 11, no. 1, pp. 79–87, 1999.

[9] P. Cardieri and T. S. Rappaport, "Application of narrow-beam antennas and fractional loading factor in cellular communication systems," *IEEE Transactions on Vehicular Technology*, vol. 50, no. 2, pp. 430–440, 2001.

[10] N. Ashraf, A. Sebak, and A. A. Kishk, "End-launch horn antenna array for ka-band 5g applications," in *2018 18th International Symposium on Antenna Technology and Applied Electromagnetics (ANTEM)*, 2018, pp. 1–2.

[11] S. Rajagopal, S. Abu-Surra, Z. Pi, and F. Khan, "Antenna array design for multi-gbps mmwave mobile broadband communication," in *2011 IEEE Global Telecommunications Conference - GLOBECOM 2011*, 2011, pp. 1–6.

[12] M. Alleven. (2017) Att debuts 5g channel sounder 'porcupine' with ni. [Online]. Available: https://www.fiercewireless.com/wireless/at-t-debuts-5g-channel-sounder-porcupine-ni

[13] C. Karpfinger, *The Dropout's Guide to PCB Trace Antenna Design*, 2010.

[14] W. L. Stutzman and G. A. Thiele, *Antenna Theory and Design*. John Wiley & Sons, 2012.

[15] M. C. Hegg and A. V. Mamishev, "Influence of variable plate separation on fringing electric fields in parallel-plate capacitors," in *Conference Record of the 2004 IEEE International Symposium on Electrical Insulation*, 2004, pp. 384–387.

[16] K. Carver and J. Mink, "Microstrip antenna technology," *IEEE transactions on antennas and propagation*, vol. 29, no. 1, pp. 2–24, 1981.

[17] M. Agiwal, A. Roy, and N. Saxena, "Next generation 5g wireless networks: A comprehensive survey," *IEEE Communications Surveys Tutorials*, vol. 18, no. 3, pp. 1617–1655, 2016.

[18] S. Rajagopal, "Beam broadening for phased antenna arrays using multi-beam subarrays," in *2012 IEEE International Conference on Communications (ICC)*, 2012, pp. 3637–3642.

[19] J. Sifri, *Design and Simulation of 5G 28-GHz Phased Array Transceiver Webcast*. Keysight Technologies, 2017.

[20] D. A. Hutchings and M. El-Shenawee, "Microwave mems antenna sensor characterization and target detection using artificial neural networks," *IEEE Sensors Journal*, vol. 14, no. 8, pp. 2461–2468, 2014.

[21] R. N. Simons, *Coplanar waveguide circuits, components, and systems*. Wiley Online Library, 2001, vol. 15.

[22] D. A. Hutchings, "Design, fabrication and testing of broadband mems antennas," Ph.D. dissertation, 2010. [Online]. Available: https://search.proquest.com/docview/305184631?accountid=8361